DOI 10.1007/s11182-023-02830-6
Russian Physics Journal, Vol. 65, No. 10, February, 2023

EFFECT OF AGING TREATMENT ON *R* TRANSFORMATION IN NANOCRYSTALLINE Ti–50.9 at.% Ni ALLOY

S. L. Girsova, T. M. Poletika, S. M. Bitter, and A. I. Lotkov UDC 69.018.6: 620.187

Effects of the size, morphology, and spatial distribution of coherent Ti_3Ni_4 *particles in a nanocrystalline* Ti–*50.9 at.%* Ni *alloy with an inhomogeneous grain-subgrain structure on the B2 → R transformation and the morphology of the R phase are studied. It has been found that the morphology of the R phase in the alloy depends on the aging temperature and changes from nanodomain observed after low-temperature aging (300°C) to lamellar self-accommodative morphology formed under conditions of intense particle precipitation (400°C). It is shown that this is due to a change in the spatial distribution of particles from location on dislocations to precipitation near low-angle boundaries. In the case of lamellar morphology of self-accommodation, the R-plates reorientation develops localized in a Lüders-like manner.*

Keywords: nanocrystalline TiNi alloy, aging heat treatment, Ti_3Ni_4 particles, martensitic transformations, *R*-phase morphology, deformation.

INTRODUCTION

Near-equiatomic TiNi shape memory alloys are of great technological interest because of their good structural and functional properties. Due to unique mechanical properties (shape memory effect and superelasticity), they are the most preferred materials for the manufacture of medical structures with complex functional properties [1, 2]. Nanocrystalline TiNi-based alloys produced by severe plastic deformation methods due to high strength and increased functional stability are used as materials for components of miniature medical systems. Generally, binary TiNi alloys with a high content of Ni atoms (50.6–50.9 at.%) are used, which are subject to aging with the formation of coherent Ti_3Ni_4 particles [1–3]. Ti_3Ni_4 precipitation leads to a change in the path of martensitic transformations from a single-stage martensitic transformation from austenite *B*2 to the monoclinic martensite phase *B*19′ through a sequence of transformations of the rhombohedral martensite phase *R*: $B2 \rightarrow R \rightarrow B19'$ [3, 4–6]. It is well known that choosing the mode of aging of the TiNi alloy with the coherent Ti_3Ni_4 particles precipitation, one can influence the intervals of martensitic transformations and functional properties. In addition to the deposition of the Ti_3Ni_4 particles, the following possible factors can lead to the formation and stabilization of the *R*-phase: the introduction of crystal defects and dislocations by hardening or thermal cycling [7], suppression of the formation of martensite with grain refinement [8], and alloying with a third element [9]. The available studies are mainly focused on the mechanical and thermal behavior of the *R*-phase [10, 11], while little information has been accumulated about the structure and morphology of the *R*-phase as well as the microscopic mechanisms of their transformation and reorientation. The purpose of this work is to obtain new knowledge about the effect of the *B*2 structure and the size and spatial distribution of the Ti_3Ni_4 particles in the nanostructure of the aged Ti–50.9 at.% Ni nanocrystalline alloy on the occurrence, transformation, and morphology of the *R*-phase being formed. In addition, the evolution of the morphology of the *R*-phase after loading-unloading cycle is investigated. This knowledge can be used to fine-tune the interval of martensitic transformations in the nanocrystalline Ni-rich TiNi alloy in the process of medical product manufacturing.

Institute of Strength Physics and Materials Science of the Siberian Branch of the Russian Academy of Sciences, Tomsk, Russia, e-mail: girsova@ispms.ru. Original article submitted December 19, 2022.

TABLE 1. Martensitic Transformation Temperatures in Ti–50.9 at.% Ni Alloy Specimens

T annealing	T_R, °C	M_s, °C	M_f, °C	A_s, °C	A_f,°C
Initial	7	–67	–134	–35	–14
300°C	34	–42	–127	–14	3
400°C	41	–29	–78	6	27

1. MATERIALS AND METHODS

A commercial nanocrystalline Ti–50.9 at.% alloy (Vascotube GmbH) was used as a research material. Samples were cut from microtubules intended for manufacturing medical stents. The samples were annealed at 300 (low-temperature aging) and 400°C (interval of intense precipitation of the Ti_3Ni_4 particles) for 1 h. The chosen temperatures make it possible to generate the Ti_3Ni_4 particles of different sizes and spatial distributions in the nanostructure. Heat treatments were carried out in a salt bath with automatic temperature control. After exposure for a specified time, the samples were quenched in water at room temperature. The critical start temperatures of $B2 \rightarrow R(T_R)$ as well as the start and finish temperatures of $B2 \leftrightarrow B19'(M_S, M_F, A_S, A_F)$ determined by resistivity measurements are presented in Table 1. Therefore, a multistage character of martensitic transformations is realized in annealed alloys. The increase in T_R temperatures indicates that the R-phase is stabilized by the titanium enrichment that occurs during the aging process [3]. Structural studies of samples cut along the direction of the tube axis by transmission electron microscopy (TEM) were performed on a JEM 2100 microscope (JEOL). The thin foil preparation procedure included grinding and mechanical polishing to a thickness of 0.1 mm, followed by ion thinning on an EM 09100IS (JEOL) ion slicer. The average size of grains and subgrains was determined by measuring the average diameter of no less than 100 grains on bright- and dark-field images. A comparative analysis of the size of the Ti_3Ni_4 precipitations in samples heat-treated at various temperatures was carried out mainly on dark-field images. The loading-unloading diagrams under tension of tubular specimens were obtained on an LFM-125 testing machine at a rate of 4×10^{-5} s^{-1}. The tensile deformation of the samples exhibited usual behavior with flat stress plateau corresponding to the propagation of Lüders-like deformation bands associated with the $B2 \rightarrow B19'$ martensitic transformation [3, 12].

2. RESULTS AND DISCUSSION

In the as-received state nanocrystalline Ti−50.9 at.% Ni alloy was in the $B2$ phase (Fig. 1) and had an inhomogeneous grain-subgrain $B2$ austenite nanostructure containing: (i) conglomerates of slightly misoriented nanosubgrains of submicron size and (ii) nanograins with high-angle boundaries included into the substructure [13]. The subgrains contain high-density dislocations and have imperfect low-angle boundaries with an azimuthal misorientation of less than 3°. The average grain/subgrain size was 80 nm. Microdiffraction patterns corresponding to the grain-subgrain structure have mainly the form of rings of separate point $B2$ austenite reflections.

After low-temperature aging at 300°C, processes of recovery and polygonization were observed, but the dislocation background in the substructure was retained, and the sizes of nanograins/subgrains changed insignificantly. The coherent Ti_3Ni_4 particles less than 10 nm in size were precipitated mainly inside subgrains on dislocations as well as in nanograins containing dislocations [14]. It is not always possible to identify the coherent Ti_3Ni_4 particles on BF images due to a weak diffraction contrast and a small volume fraction of precipitations (Fig. 2*a*). In this case, the Ti_3Ni_4 particle precipitation was indicated by the presence of weak reflections on the SAED patterns at the 1/7 positions along the directions of the $B2$ <321> lattice (Fig. 2*b*). There are widened size ranges of polygonized nanograins/subgrains in the temperature range of high-intensity aging (400°C) (Fig. 2*d–f*). High dislocation density can be seen in the BF, indicating that recrystallization has not set in. The size of the Ti_3Ni_4 particles increases and their shape approaches lenticular with a transverse size of up to 15 nm and a length of up to 35 nm. The spatial distribution of the Ti_3Ni_4

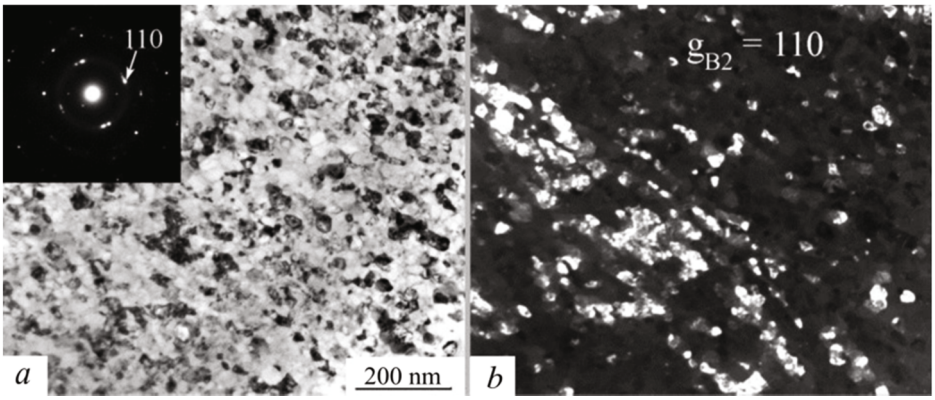

Fig. 1. Grain–subgrain structure of the initial Ti−50.9 at.% Ni: *a*) bright-field image (BF) and selected area electron diffraction pattern (SAED) in the inset, and *b*) dark-field image (DF) in *B*2 {110} reflection in (*a*).

particles in the substructure changes from location at dislocations to precipitation at subboundaries (Fig. 2*e*). In this case, the Ti_3Ni_4 particles tend to line up in the {111} planes, which indicates the autocatalytic character of nucleation [6]. Note that the effect of aging is practically not observed in nanograins, which is associated with geometric restrictions from the high-angle boundaries [15].

After annealing at 300 and 400°C, the investigated alloy is in the $B2 + R$ two-phase state (Table 1). It is assumed that the *R*-phase emerges around the coherent Ti_3Ni_4 precipitates: (i) near the boundary between the *B*2 matrix and the Ti_3Ni_4 precipitate, which is associated with the lowest Ni concentration in this region, and (ii) internal stress associated with the coherent Ti_3Ni_4 precipitates [4 – 6, 10, 11]. The high density of dislocations and Ti_3Ni_4 precipitates can act as a medium for the nucleation of the *R*-phase in the alloy during low-temperature aging at 300°C. The *R*-phase typical extra spots of 1/3 ⟨321⟩ *B*2 type can be seen on the SAED patterns (Fig. 2*b* and *e*). The DF image of the *R*-phase structure after annealing at 300°C (Fig. 2*c*) shows that the *R*-phase has the nanodomain-like structure instead of commonly observed plate form [16]. The domains are spherical, up to 8 nm in size, and are located in subgrains and nanograins containing the Ti_3Ni_4 precipitates. It is believed that in the *B*2 matrix containing the coherent Ti_3Ni_4 precipitates and high-density dislocations, the space for the transformation of the *R*-phase is strongly limited. In this case, due to the presence of local fields of internal deformations/stresses in small-scale constrained conditions, the formation of the *R*-phase in the morphology of nanoprecipitates is possible [17, 18]. Figure 2*f* shows the *R*-phase morphology observed after annealing at 400°C. The DF image shows that the *R*-phase morphology feature is the sticking of individual *R* precipitations and their subsequent coalescence into plates of the *R*-phase. In this case, the *R*-plates with a habit close to {110} *B*2 predominate (Fig. 5*f*).

In the TiNi alloys, the formation of the *R*-phase domains is rarely observed. An example may be nanocrystalline TiNi containing high density of dislocations or precipitates which differ in that the free space for the martensitic transformation in them is very limited. This imposes a significant limitation and causes resistance to deformation upon transformation. As a result, the high elastic energy is accumulated, which contributes to the loss of the self-accommodation morphology of the martensitic phase [17–19]. With a change in the conditions of *R*-phase formation during heat treatments (including the density of defects and the particle sizes), its phase morphology will also change. The release of the internal space of subgrains from dislocations and Ti_3Ni_4 precipitates with increasing aging temperature leads to the appearance of a self-accommodative lamellar form of the *R*-phase [20]. This indicates that the internal stress plays a dominant role in the formation of self-accommodating *R*-phase structures.

Fig. 3 shows the structure of the aged samples after loading-unloading cycle. The BF image of the structure after annealing at 300°C (Fig. 3*a*) shows that the *R* transformation develops homogeneous since the *R* martensite plates are formed in all grains/subgrains almost regardless of their sizes and orientation. The *R* plates in substructure regions and in nanograins form specific configurations with preferential crystallographic orientations favorable to the external

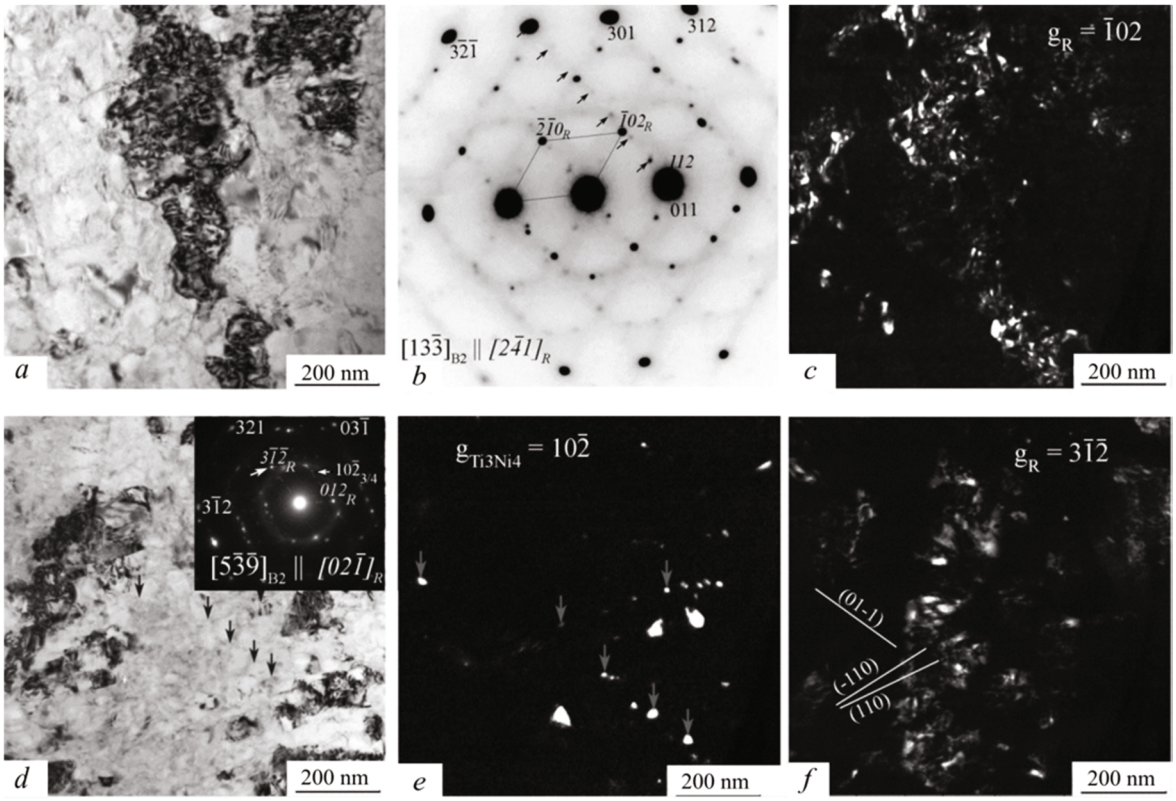

Fig. 2. Ti−50.9 at.% Ni alloy structure after annealing at 300 (*a–c*) and 400°C (*d–f*): *a*) substructure BF image; *b*) corresponding SAED pattern in which the zone axes $Z_{B2} = [13\bar{3}]$ and $Z_R = [2\bar{4}1]$ parallel to the incident electron beam are indexed, dark arrows show reflections of the Ti_3Ni_4 particles in positions 1/7 along the *B*2 lattice directions $[\bar{3}21]_{B2}$, and the *R*-phase reciprocal lattice section is highlighted by lines; *c*) DF taken in the reflection of the *R*-phase indicated by the arrow on SAED; *d*) BF of the subgrain structure; *e*) DF taken in the Ti_3Ni_4 $\{10\bar{2}\}$ reflection marked by the arrow in (*d*); arrows in (*d*) and (*e*) indicate the particles visible on the Ti_3Ni_4 $\{10\bar{2}\}$ reflection in the microdiffraction pattern in (*d*); and *f*) DF image in the $\{3\bar{1}\bar{2}\}$ *R*-phase reflection; traces of planes corresponding to the *R*-phase habitus planes are marked with lines on DF (*f*).

stress fields. Note that the strain-induced *R* martensitic plates were able to go across the whole grains/subgrains or substructure regions (Fig. 3*a*).

Figure 3*b* shows the DF image of the *R*-phase in a single grain in the (110) reflection on the SAED pattern, which allows considing the internal structure of the plates. It can be seen that the evolution of individual *R* precipitates during the deformation cycle is related to sticking of individual *R* precipitates and coalescence into plates of the *R*-phase. In this case, reorientation of the *R*-phase or disappearance of its unfavorable variants and the appearance and growth of favorable variants are possible [9, 10]. Figure 3*c–f* shows the structure of the samples aged at 400°C after loading-unloading cycle. Figure 3*c* illustrates the BF image of the sample annealed at 400°C showing that the *R* transformation occurs due to the formation of plates within groups of several closely oriented subgrains. The applied stress led to an increase in the thickness of the *R*-plates to 20–30 nm. The groups of subgrains that have undergone a transformation are shown in Fig. 3*c*. The traces of the habits planes of the *R*-phase predominantly close to $\{110\}_{B2}$ are marked by white lines. The images obtained suggest that the R transformation in subgrains is a cooperative process in which local stress in the transforming subgrain will promote the strain-induced $B2 \leftrightarrow R$ transformation or *R* reorientation in the neighboring subgrains. Figure 7*e* shows the BF image of the structure that demonstrates the cooperative effect. Large elongated agglomerates of subgrains, containing the *R*-plates with certain orientations, are

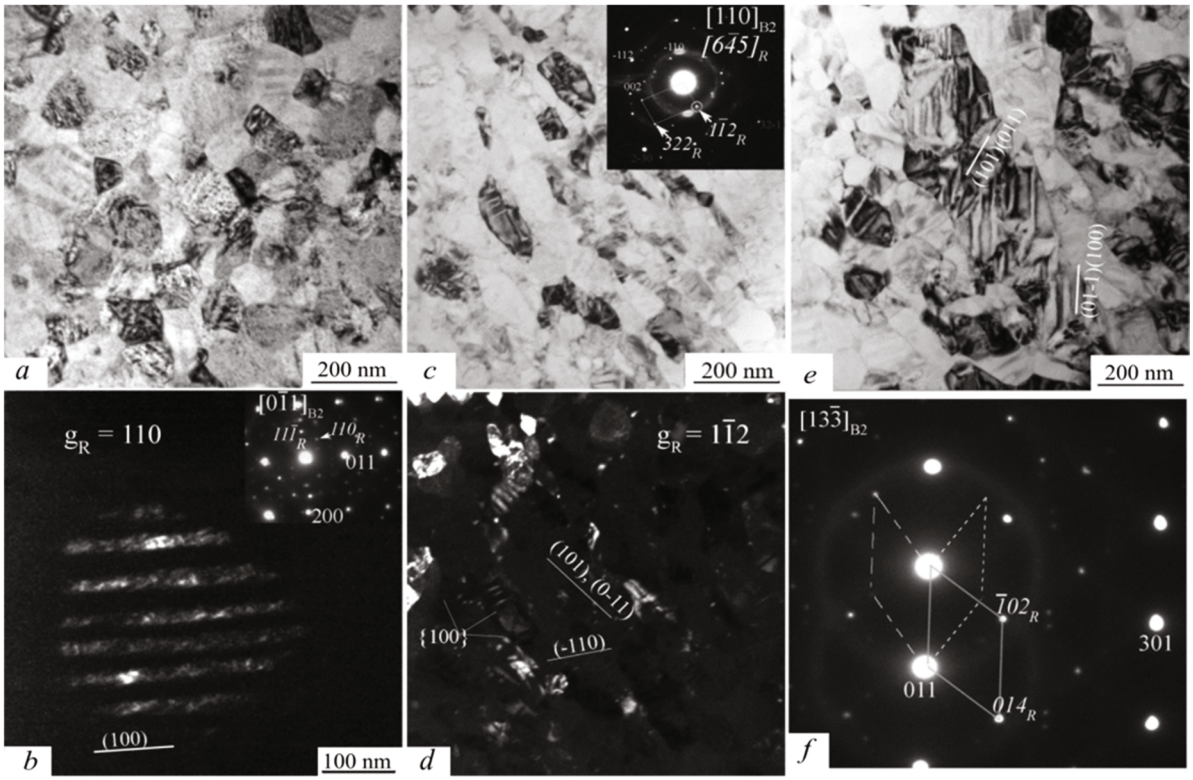

Fig. 3. Ti−50.9 at.% Ni alloy structure after annealing at 300 (*a* and *b*) and 400°C (*c–f*) and loading-unloading cycle: *a*) BF of the grain-subgrain structure; *b*) DF of *R*-phase plates and the corresponding SAED, where $Z_{B2} = [0\bar{1}1]$ and one of the three variants of the *R*-phase present on the SAED with $Z_R = [\bar{1}10]$ are indexed; *c*) BF with the corresponding SAED in the inset; *d*) DF taken in the reflection of the *R*-phase indicated by the arrow on the SAED, where traces of planes corresponding to the *R*-phase habitus planes are marked; *e*) BF*; f*) SAED, where $Z_{B2} = [13\bar{3}]$ and $Z_R = [2\bar{4}1]$ (solid line) are indexed, and the dashed straight lines highlight the lattices of two *R*-phase variants in a twin ratio with $Z_R = <201>$.

visible. It was observed that the strain-induced or reoriented *R*-plates were able to go across the whole subgrains in the direction favorable to the external loading axis. White lines mark traces of planes corresponding to the habit planes of the *R*-phase. The SAED pattern (Fig. 7*f*) in the zone axes $Z_{B2} = [13\bar{3}]$ and $Z_R = [2\bar{4}1]$ (solid lines) are indexed, the dashed lines highlight the lattices of two *R*-phase variants in twin orientation whith $Z_R = <201>$. Obviously, the agglomerates of subgrains observed are elongated in the direction favorable to the external loading axis. In this case, the variant of subgrains with the highest resolved shear stresses are formed first, and the strain-induced or reoriented *R* plates trigger the formation of like variants in similar directions in neighboring grains. We assume that this behavior provides the localized stress-induced *R* transformation in a Lüders-like manner [21, 22].

CONCLUSIONS

The research has been focused on the *R*-phase and its morphology formed under conditions of a defect structure containing dislocations and the Ti_3Ni_4 nanoparticles. It was found that the size and spatial distribution of the Ti_3Ni_4 particles significantly affect the morphology of the *R*-phase during the $B2 \rightarrow R$ transformation. It was established that there is a change in the morphology of the *R*-phase from the nanodomains in the alloy after low-temperature aging at 300°C to the lamellar self-accommodative morphology in the alloy aged under conditions of intense particle

precipitation at 400°C. It is shown that this is due to the change in the spatial distribution of particles from location on dislocations to precipitation near low-angle boundaries.

After low-temperature annealing at 300°C, a homogeneous nanostructure was formed with grains/subgrains containing both dislocations and the Ti_3Ni_4 particles and nanodomains of the *R*-phase located within a highly confined space. The *R* transformation and reorientation under applied stress develop locally in individual grains/subgrains due to the reorientation of the *R*-phase particles and their coalescence into larger plates oriented in the direction favorable to the external loading axis, thereby ensuring uniform deformation.

After annealing at 400°C, the nature of the *R* transformation changed to the formation of the *R*-plates. Under loading in the substructure, an easily occurring reorientation of the *R* plates was observed, leading to the formation of lamellae formed from conglomerates of subgrains and elongated in the direction favorable to the axis of external loading. We believe that the growth of lamellas occurs due to the formation and coalescence of identical variants in similar directions in neighboring grains. First, subgrain variants with the highest allowed shear stresses are formed. Strain-induced or reoriented *R* plates cause the formation of variants in similar directions in neighboring grains. This behavior is very similar to the stress-induced localized Lüders-like *R* transformation. The mechanisms of the observed processes require further study and discussion.

This work was carried out within the framework of the Government Research Assignment for the ISPMS SB RAS (Project No. FWRW-2021-0004).

REFERENCES

1. M. H. Elahinia, M. Hashemi, M. Tabesh and S. B. Bhaduri, Prog. Mater. Sci., **57**, 911–946 (2012).
2. A. R. Pelton, S. M. Russel, and J. DiCello, JOM, **55**, 33–37 (2003).
3. K. Otsuka and X. Ren, Prog. Mater. Sci., **50**, 511–678 (2005).
4. Y. Zheng, F. Jiang, L. Li, *et al*., Acta Mater., **58**, 3444–3458 (2010).
5. G. L. Fan, W. Chen, S. Yang, *et al*., Acta Mater., **52**, 4351–4362 (2004).
6. J. Khalil-Allafi, X. Ren, and G. Eggeler, Acta Mater., **50**, 793–803(2002).
7. A. S. Mahmud, Z. Wu, H. Yan, and Y. Liu, Shape Mem. Superelasticity, **3**, 57–66 (2017).
8. T. Waitz, V. Kazykhanov and H. P. Karnthaler, Acta Mater., **52**, 137–147 (2004).
9. S. Miyazaki and K. Otsuka, Phil. Mag. A, **50**, 393–408 (1984).
10. X. Wang, B. Verlinden, and J. Van Humbeeck, Mater. Sci. Tech., **30,** 1517–1529 (2014).
11. T. W. Duerig and K. Bhattacharya, Shape Mem. Superelasticity, **1**, 153–161 (2015).
12. P. Šittner, M. Landa, P. Lukáš, and V. Novák, Mech. Mater., **38**, 475–492 (2006).
13. S. Prokoshkin, V. Brailovski, S. Dubinskiy, *et al*., Shape Mem. Superelasticity, **2**, 12–17 (2016).
14. T. M. Poletika, S. L. Girsova, and A. I. Lotkov, Intermetallics, **127**, 106966 (2020).
15. E. A. Prokofiev, A. Burow, E. Payton, and S. Bhaduri, Adv. Eng. Mater., **12**, 747–753 (2010).
16. S. Miyazaki and C. M. Wayman, Acta Metal., **36**, 181–192 (1988).
17. T. Fukuda, T. Saburi, K. Doi, and S. Nenno, Mater. Trans. JIM, **33**, No. 3, 271–277 (1992).
18. Y. Chen, Y. Liu, K. Yu. F. Yang, *et al*., Materialia, **20**, 101262 (2021).
19. X. Huo, P. Chen, S. Lahkar, *et al*., Acta Mater., **227**, 117688 (2022).
20. P. M. Petersmann, W. Pranger, T. Waitz and T. Antretter, Adv. Eng. Mater., **19**, 1–6 (2017).
21. S. C. Mao, J. F. Luo, Z. Zhang, *et al*., Acta Mater., **58**, 3357–3366 (2010).
22. B. Feng, X. Kong, S. Hao, *et al*., Acta Mater., **194**, 565–576 (2020).